Available online at www.sciencedirect.com
ScienceDirect
International Journal of Heat and Mass Transfer 49 (2006) 4721–4731
International Journal of HEAT and MASS TRANSFER
www.elsevier.com/locate/ijhmt

In situ investigation of water transport in an operating PEM fuel cell using neutron radiography: Part 2 – Transient water accumulation in an interdigitated cathode flow field

J.P. Owejan [a,*], T.A. Trabold [a], D.L. Jacobson [b], D.R. Baker [a], D.S. Hussey [b], M. Arif [b]

[a] General Motors Fuel Cell Activities, 10 Carriage Street, Honeoye Falls, NY 14472, USA
[b] National Institute of Standards and Technology (NIST), Center for Neutron Research, 100 Bureau Drive, Gaithersburg, MD 20899, USA

Received 18 May 2005; received in revised form 30 June 2006
Available online 20 September 2006

Abstract

An interdigitated cathode flow field has been tested in situ with neutron radiography to measure the water transport through the porous gas diffusion layer in a PEM fuel cell. Constant current density to open circuit cycles were tested and the resulting liquid water accumulation and dissipation rates with in-plane water distributions are correlated to measured pressure differential between inlet and outlet gas streams. The effect of varying the reactant gas relative humidity on liquid water accumulation is also demonstrated. These results provide evidence that the reactant gas establishes a consistent in-plane transport path through the diffusion layer, leaving stagnant regions where liquid water accumulates. A simplified permeability model is presented and used to correlate the relative permeability to varying gas diffusion layer liquid water saturation levels.

Keywords: Fuel cell; Interdigitated; Neutron radiography; Visualization; Water management

1. Introduction

In a polymer electrolyte membrane (PEM) fuel cell, the gas diffusion layer has stringent design constraints. It must be porous, thermally and electrically conductive, mechanically stable under compression, and able to support three-dimensional diffusion and water removal. Optimization of these material properties is especially important for the cathode side of the fuel cell, due to the relatively slow kinetics of the oxygen reduction reaction. Interdigitated reactant flow fields have been developed and employed in PEM fuel cells to aid in water management by forced convective transport through the diffusion layer [1–4]. In this flow field design, the reactant channels are not continuous from inlet to outlet, but are rather terminated to force gas through the diffusion layer.

Product water may be removed from the cathode electrode by several mechanisms: back diffusion to the anode, membrane uptake, diffusion (with less than 100% saturated inlet gas stream used), and condensation with capillary transport. These combined mechanisms are responsible for introducing liquid water into the gas diffusion layers. Once liquid water is accumulated in the cathode diffusion layer it is removed by evaporation, capillary transport and shear drag force from convective flow through the flow field channels across the surface of the diffusion layer. Liquid water in the anode diffusion layer is of lesser

* Corresponding author. Tel.: +1 585 624 6802; fax: +1 585 624 6680.
E-mail address: jon.owejan@gm.com (J.P. Owejan).

0017-9310/$ - see front matter © 2006 Elsevier Ltd. All rights reserved.
doi:10.1016/j.ijheatmasstransfer.2006.07.004

Nomenclature

$A_{x-\mathrm{DL}}$	diffusion layer substrate cross-sectional area, cm^2
d	source aperture, m
d_{ch}	channel width, cm
d_{land}	land width, cm
F	Faraday constant, 96485.34 sA/eq
GDL	gas diffusion layer
h	cathode gas diffusion layer thickness, cm
h_{ch}	channel depth, cm
HFR	high frequency resistance, $\Omega\,\mathrm{cm}^2$
J	current density, $\mathrm{A/cm}^2$
k	gas phase permeability, darcy
l	channel length, cm
L	beam length, m
MEA	membrane electrode assembly
MPL	microporous layer
N	atomic density, molecules/cm^3
n_{ch}	number of channels
n_{land}	number of lands
P	pressure, Pa
$\overline{P}'_1(0)$	dimensionless inlet gas velocity
R_{ch}	hydraulic radius of channel, cm
RH	relative humidity, %
s	saturation ratio
t	time, s
T	thickness, cm
V_i	velocity in channel i, cm/s
V_{land}	velocity in land, cm/s
V^{vol}	volumetric gas flow, cm^3/s
Greek symbols	
α	ratio of convective resistance to gas flow
μ	gas viscosity, Pa s
Φ	gas diffusion layer substrate porosity

concern considering the high diffusivity of hydrogen. Use of an interdigitated design in the cathode flow distributor will increase liquid water removal from the cathode diffusion layer through convective transport.

Such a design has several shortcomings from a system and durability perspective. The increased pressure differential induced by forcing all gas flow through the relatively low permeability gas diffusion layer will result in increased compressor work and hence reduced system efficiency. However, the interdigitated design is a proven tool for in situ water management diagnostics and characterization. At the onset of load, during the initial transition from open circuit, it has been shown that cathode pressure drop will increase proportionally with product water mass as it is generated from the oxygen reduction reaction [3].

Upon reviewing the available data it is speculated that water accumulation in both the flow channels and the diffusion layer can be correlated to the pressure drop behavior on the cathode side of the fuel cell. Moreover, it suggests that the rate at which the pressure differential increases is proportional to the water production rate, and that the gas diffusion layer accumulates water until a critical void is filled. At this point, the pressure drop stops increasing and the mass flow rate of water removed from the cell matches the rate at which water is produced. It is expected that this "critical water mass" can be optimized by varying diffusion layer parameters to reduce the percentage of voids blocked with stagnant liquid water, thereby decreasing the mass transport resistance.

Coupling neutron radiography with an interdigitated cathode flow field and pressure differential measurements can offer insight into local water accumulation, and enable quantification of the critical mass that will be retained in the cell. The present paper describes the application of this technique to study a single $50\,\mathrm{cm}^2$ PEM fuel cell, and expands upon the detailed description of the experimental method provided in the Part 1 paper [5]. In contrast to previous applications of neutron radiography in fuel cell studies [6–11] these experiments are focused on using the method to obtain unknown saturation relationships in the gas diffusion layer (GDL). Water production rates (at constant current density) are compared to water retention rates in diffusion layer and separately in the flow field channels. Also, the ohmic resistance is correlated to inlet relative humidity and saturation level of the diffusion layer.

2. Experimental

The experimental apparatus has been changed somewhat from that in Part 1 of this study. This modification (described in detail in [12]) involves moving the testing area downstream of the previous test area by a distance of 2.13 m and adding an additional 5 cm of liquid nitrogen cooled bismuth filter material before the collimating aperture. Moving the apparatus results in an increase in the beam size at the sample position from 18 cm to 26 cm. This reduces the thermal neutron fluence rate to 43% of the previous value. The additional 5 cm of bismuth reduces background high-energy neutrons and gammas at a cost of reducing the thermal neutron fluence rate to a further 58% of the previous value. Overall the total fluence rate has been reduced to 25% of the previous value. On the other hand, to recover the intensity, the full open or 2 cm aperture position was used, which provided a factor of 4 increase in intensity. Previously the 2 cm aperture could not be used since the background fast neutron and prompt gamma radiation level were too high for the existing shield-

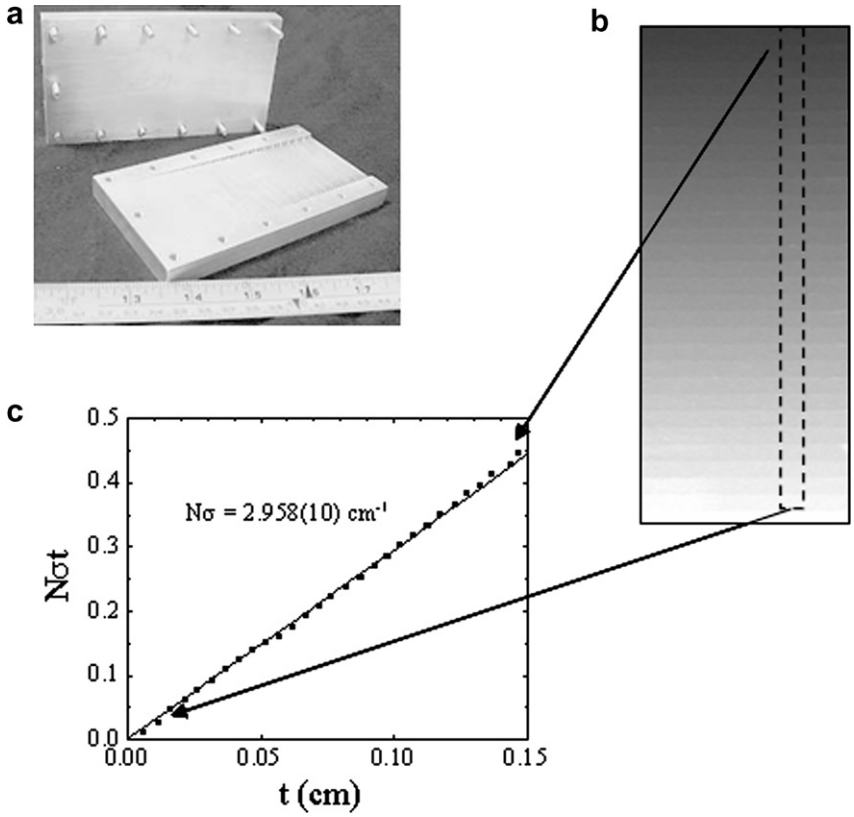

Fig. 1. Water macroscopic neutron cross-section calibration cuvette.

ing to provide adequate radiological protection. The additional 5 cm of bismuth helped to lower this background to acceptable levels. The last alteration was to the L/d ratio, which changed from 400 to 300. An L/d ratio of 300 is considered to be very good for a neutron fluence rate of $1.84 \times 10^7\ \mathrm{cm^{-2}\ s^{-1}}$.

An additional calibration of the water mass as measured by neutron transmission is also presented here. To convert the attenuation images (representing the product $N\sigma T$, as described in Part 1 [5]) to water mass values or thickness values, the attenuation length ($N\sigma$) must be known. The value for σ depends on energy and thus the attenuation length depends on the neutron beam spectrum. Here the neutron beam is a thermal Maxwellian distribution of neutrons and therefore the cross-section is averaged over the many different neutron energies found in this beam. Based on a Monte Carlo N particle (MCNP) calculation of the beam spectrum [12] and measured liquid water cross-sections as a function of energy [13], the average calculated cross-section is $3.197\ \mathrm{cm^{-1}}$. To avoid uncertainty in the MCNP calculation, the cross-section for water for this beam is measured. In addition the cross-section measurement demonstrates the linearity of the measured values, which is essential for application of Beer's law. Fig. 1 shows the device constructed to allow many thicknesses of water to be placed in the beam. It consists of many steps machined into an aluminum plate with each step approximately 50 μm thicker than the previous step. The true step size was measured with a Mitutoya digital indicator[1] with 1 μm resolution. Fig. 1 shows the average gray level image versus the measured step thickness of the water. From the slope of a linear least squares fit of the data in Fig. 1 the value of the attenuation coefficient $N\sigma$ is determined to be $2.958 \pm 0.010\ \mathrm{cm^{-1}}$.

The fuel cell experimental apparatus is generally unchanged from that described in Part 1 of this study. The only notable change in the test section is the anode and cathode flow distributor designs. The anode is a straight pass design that was not interdigitated and the cathode is a straight pass with interdigitated channels. Fig. 2 gives an overview of the cathode flow field design where every other channel has an inlet and the remaining channels are connected to the outlet manifold. This design forces convective transport through the diffusion layer. The anode flow distributor dimensions are identical, except that every channel is connected to both the inlet and outlet headers. The anode and cathode flow channels are 1.42 mm wide and 0.3 mm deep, with a land width between of 2.68 mm. Both flow fields were machined from aluminum

[1] Certain trade names and company products are mentioned in the text or identified in an illustration in order to adequately specify the experimental procedure and equipment used. In no case does such identification imply recommendation or endorsement by the National Institute of Standards and Technology, nor does it imply that the products are necessarily the best available for the purpose.

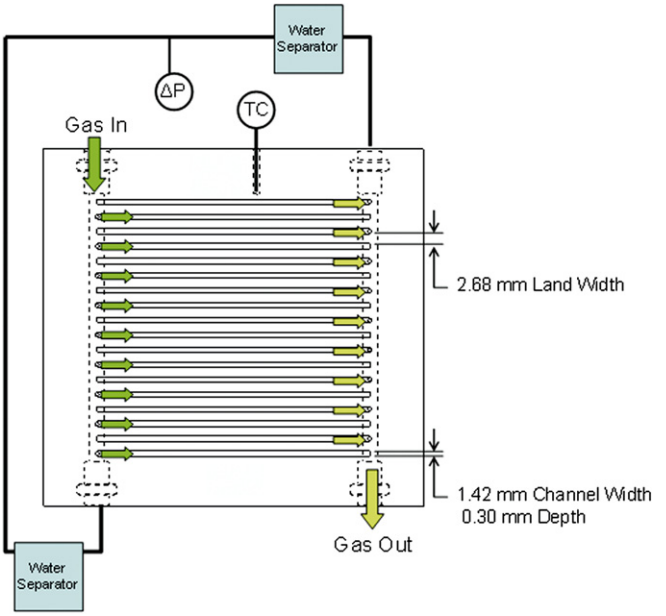

Fig. 2. Cathode interdigitated flow field.

and then plated with a thin layer of gold. These materials have relatively low neutron attenuation, and were selected to enhance the sensitivity of the measurement system to liquid water produced within the fuel cell.

Differential pressure is measured directly from the inlet and outlet headers with 40 kPa differential pressure sensors. The pressure sensors are calibrated and accurate within an uncertainty band of ±0.25 kPa. The cell temperature is controlled by a thermocouple located in the cathode flow field (not the backing plate). Measurements of all operating parameters (flows, temperatures, pressures, voltage, current, and impedance amplitude) are acquired at a frequency of 1.0 Hz.

After the cell had undergone a start-up procedure to hydrate the membrane, all experiments were run in constant current mode to assure a constant water production rate in the cell. A low load of 0.2 A/cm^2 that is of interest for these experiments was ideal to assure that the temporal resolution (0.18 Hz) of the neutron imaging system would capture the water generation dynamics during the transient experiments. These experiments consist of load cycling (off–on–off) with constant reactant gas flow. Additional inlet relative humidity (RH) transients were conducted at continuous load. In these experiments the inlet RH was decreased from 100% to 50% and back again. The outlet pressure was fixed in all experiments at 120 kPa.

In all tests the anode and cathode gas flow was run continuously with a stoichiometric ratio (i.e., ratio of the actual flow to that required by reaction stoichiometry) of 2.0, calculated based on load. The load cycling tests were run with the cell temperature maintained at 60 °C and the anode and cathode dew points were maintained at 60 °C resulting in 100% saturated inlets. This condition was used to minimize evaporation and back diffusion, hence isolating convective and capillary transport in the cathode backing layer. The RH transient experiment was executed by keeping the cathode dew point constant at 60 °C and increasing the cell temperature and the anode dew point to 76 °C, in turn varying the cathode inlet RH from 100% saturated to 50%.

Radiographs were exposed for 2 s each with an image file write time of 3.41 s resulting in the temporal resolution of 0.18 Hz. The CCD camera was focused on a 10 cm × 10 cm area. The camera was a large format 2048 × 2048 pixel camera, but the images were binned to 1024 × 1024 because the spatial resolution constraining component was the scintillator, not the CCD array. By reducing the image size each pixel had a similar spatial resolution to that of the scintillator, which is described in more detail in Part 1 [5,12].

3. Results and discussion

Radiographs were averaged typically in groups of 10 images to increase the signal-to-noise ratio for both visual and quantitative analysis. Since the background CCD signal (no neutron flux) is typically constant and accounted for in the image analysis, the primary contributor to noise in individual images is scattered neutrons. After averaging a sequence, a median filter with a 3 × 3 kernel was applied to remove hot, dead pixels, and data from fast neutrons. Averaging images, however, greatly reduced temporal resolution and as a result the data are presented in the form of average accumulated water.

With saturated inlet gas streams, condensation in the gas delivery system existed even though efforts were made to minimize this effect. Condensation is a result of fluctuations in PID (proportional integral derivative) temperature control and cold spots in the heated delivery lines. Through transient analysis of sequential radiographs (movies) it was possible to isolate accumulated water from inlet condensation. This has been considered in all quantitative analyses of the presented data, where condensed water was not considered in measurements. This issue is expected to be a problem with most humidification systems for fuel cell testing, and it has been observed in these experiments that even very small amounts of condensation have a significant effect on channel water accumulation in small-scale systems. In the configuration presented in this paper, most accumulation from condensation was in the anode channels due to the straight pass, low velocity and pressure drop. These random slugs in the anode channels are not expected to affect the fuel cell experiments given the small relative length scale of the blockage.

3.1. Load cycling global water accumulation and dissipation

Recent publications have shown that the cathode pressure differential in an interdigitated flow field is related to water accumulation and dissipation associated with the onset and offset of current load being drawn from the

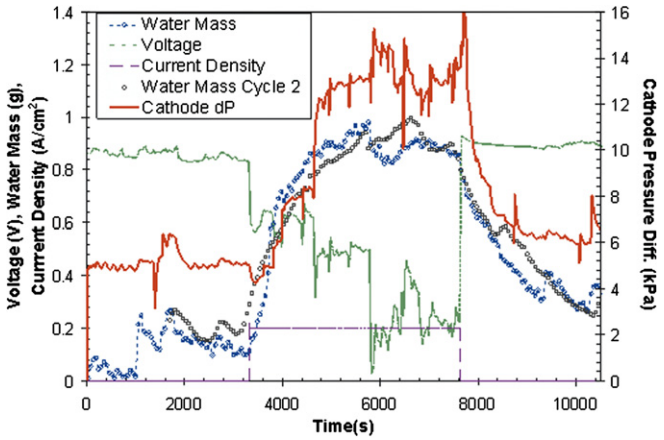

Fig. 3. Water mass, cell voltage, and cathode pressure drop response during load cycle.

PEM fuel cell [3]. Neutron radiography was used in similar experiments presented in this paper to determine the water accumulation patterns in the interdigitated design. It was suspected that the interdigitated dead-ended channels would accumulate water in the low-pressure region furthest from the inlet of the channel. It was also initially thought that this channel flooding was a contributing factor to the cathode pressure differential increase, not only saturation of the porous gas diffusion layer.

Low load (0.2 A/cm^2) water accumulation was the focus of these experiments. It is expected using load equivalent flow that the lower channel velocity and the corresponding lower pressure differential will provide a more sensitive baseline for pressure increases resulting from stagnant slugs and droplets forming in the channels and gas diffusion layer pores. Instability in the pressure signal is a result of small amounts of product and condensed liquid water in the exit lines.

The water mass values presented in Fig. 3 were calculated as outlined in Part 1 based on the CCD pixel spatial resolution (94 μm) and the change in transmitted neutron energy (density of water calculated to be 0.985 g/cm^3). Each data point represents an average of 10 images or 54.1 s of run time. The water mass never reaches a value of zero due to the small amounts of condensation previously described. At the onset of load ($t = 3320$ s), the water mass across the active area of the cell clearly begins to increase rapidly. The cathode pressure differential increases proportionally with water mass until a critical water mass is reached and then cathode pressure differential stops increasing. At this point in the data set the cell potential decreases significantly and becomes unstable, signifying a mass transport limitation has been reached as a result of product water accumulation, restricting oxygen transport to the catalyst sites.

At 0.2 A/cm^2, a 50 cm^2 active area PEM fuel cell will generate a water mass flow of 0.93 mg/s (water flux = $J/2F$; one mole of water for every mole of hydrogen reacted). Electro-osmotic drag will have a negligible contribution to product water at 0.2 A/cm^2 and will not be considered in this evaluation. The data enable a comparison between the rate at which water is produced and the rate

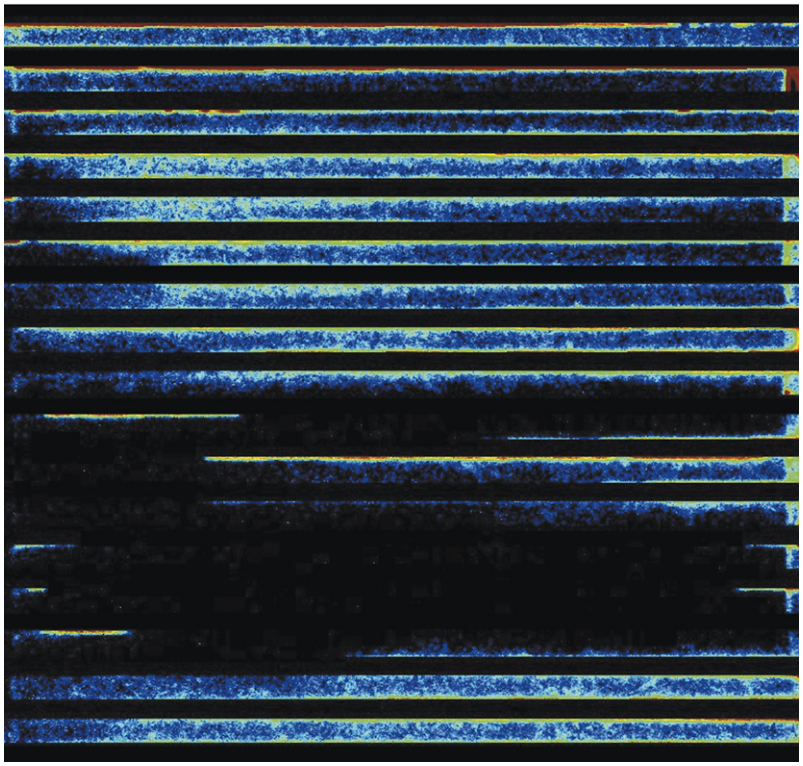

Fig. 4. Masking water measured in the channels.

at which it is accumulated in the voids of the cathode diffusion layer. A linear regression was calculated for the first 800 s after the load was activated (denoted by the first 14 data points and the steep linear increase after $t = 3320$ s). The slope illustrates the cell initially retains 0.78 mg/s of water, indicating that 84% of the water produced stays in the cell until a critical open volume of the diffusion medium is full and the induced pressure differential is sufficient to remove the water flux produced. At this point ($t = 5800$–7600 s), water accumulation in the cell reached a steady state value of 0.88 ± 0.04 g. This value includes water in the cathode diffusion medium and water in the cathode channels, which together have a total dry open volume of 1.395 cm^3.

It is possible to isolate the water accumulated in just the cathode gas diffusion layer (assuming no water in anode diffusion layer and electrodes) by performing the masking operation described in Part 1. After masking the channels the critical water mass measured in the lands is 0.23 ± 0.01 g. The land regions cover 32.4 cm^2 of the 50 cm^2 active area. The open void volume of the 75% porous gas diffusion layer (GDL) in this portion of the active area is 0.404 cm^3, accounting for only the cathode GDL thickness loaded with 20% compressive strain (compressed thickness = 166 μm, not including the MPL). On average, the maximum critical water mass in the GDL is reached once $44.2 \pm 2.5\%$ of the open void volume is filled (subtracting the estimated maximum uptake in membrane, 30% by mass) with accumulated liquid water in the cathode GDL. These void fractions were verified with subsequent cycling tests within 5% repeatability from the mean; a repeated data set is overlaid on Fig. 3 to demonstrate this repeatability. Fig. 4 shows an example of data where water in the land areas was isolated. Fig. 5 presents a series of 54 second-averaged radiographs (without channel mask) sequenced from the onset of current load. In this sequence, it is observed that the flow pattern through the GDL is non-uniform and established early in the current cycle, indicating that liquid water may be accumulating in areas of low in-plane gas velocity.

In each cycle the load was drawn from the cell for about 70 min and then the cell was set to open circuit with load-based flow for 0.2 A/cm^2 at a stoichiometric ratio of 2 on anode and cathode kept constant throughout (anode flow = 140 sccm, cathode flow = 333 sccm). In the open circuit (drying) portion of these cycles, the mass rate of water pushed out of the gas diffusion layer by gas drag force is calculated using a linear assumption (Fig. 3). At open circuit and with saturated inlet gas flow, many of the variables associated with mass transfer through the porous diffusion layer are eliminated. Removal of liquid water from the system is assumed to be purely convective;

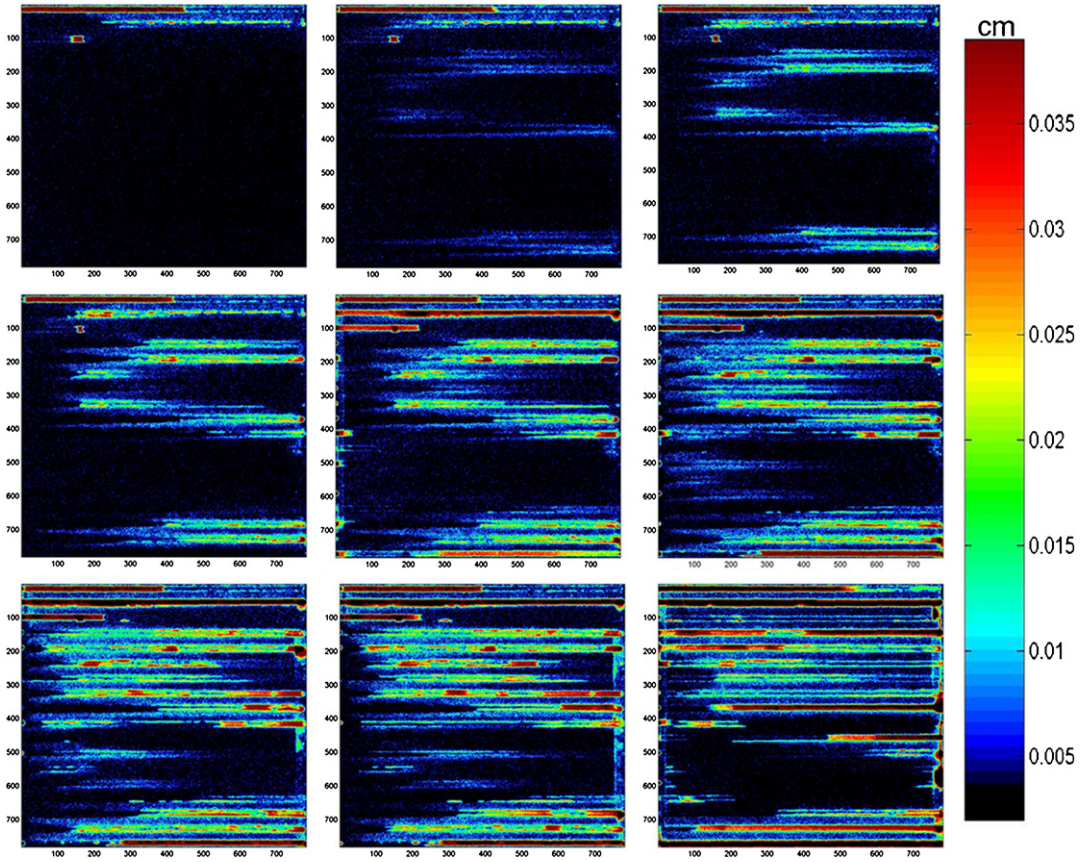

Fig. 5. Neutron radiographs showing water accumulation after onset of PEMFC reaction.

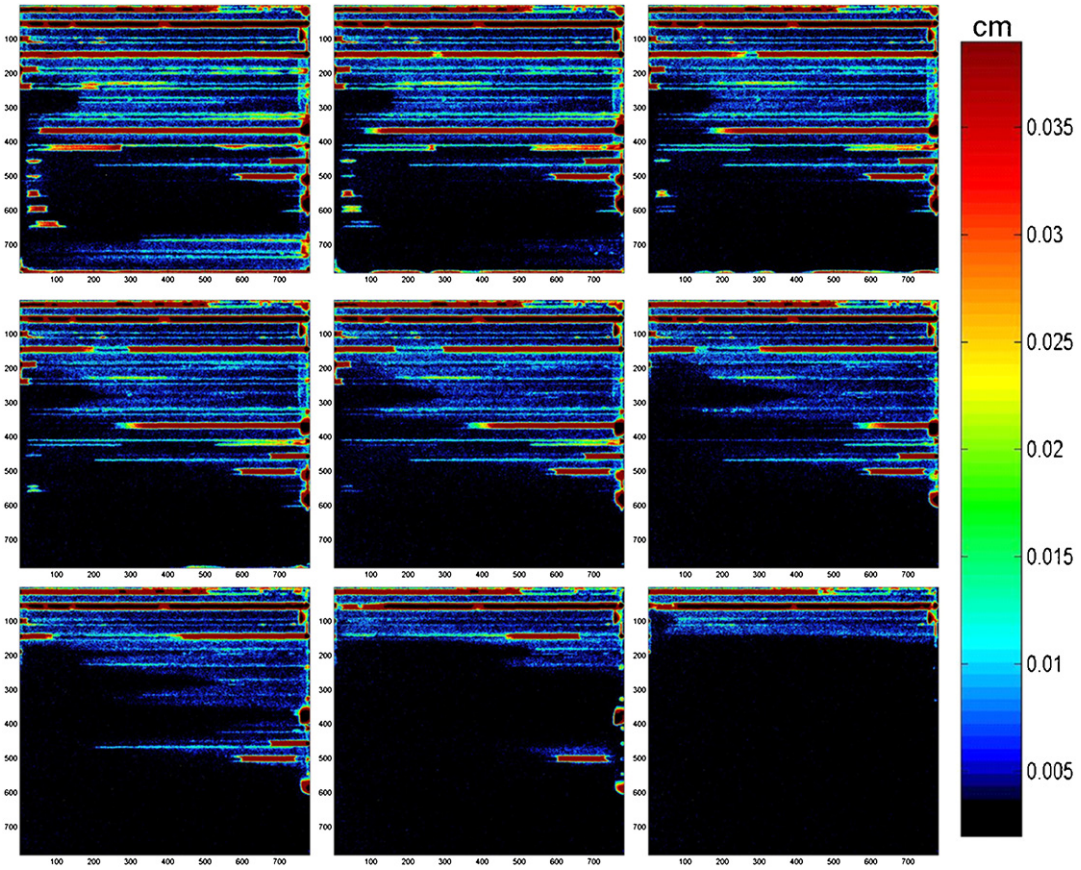

Fig. 6. Neutron radiographs showing water dissipation after offset of PEMFC reaction.

evaporation and back diffusion are neglected. The measured water dissipation flux is 0.29 ± 0.01 mg/s including channels and 0.08 ± 0.01 mg/s excluding the channel water volume, only considering the cathode GDL. Fig. 6 presents the series of 54 second-averaged radiographs (without channels mask) sequenced from the offset of current load with sustained constant gas flow.

Characterizing the convective portion of transport in the gas diffusion layer is desirable due to local water accumulated in regions associated with the diffusion layer irregularity during an actual reaction with water production. Typically this characterization must be done ex situ. The average gas velocity through the cathode gas diffusion layer substrate based on dry porosity is calculated to be 3.3 cm/s ($V^{\text{vol}}/(A_{x-\text{DL}}{*}n_{\text{land}}{*}\Phi)$). The corresponding gas volumetric flow rate through the GDL is 5.03 cm^3/s. The difference between the dissipation rate measured with neutron radiography and the gas purging volumetric flow illustrates that convective transport through the gas diffusion layer is nonhomogeneous. Homogeneous convective flow would remove water at a similar rate to the gas flow if the gas momentum was distributed evenly through the diffusion layer void. It is expected that the water trapped in the smaller pores of the gas diffusion layer cannot be removed by gas shear at the given mass flow rate. Since the pressure differential to remove a droplet is proportional to both the radius of curvature and surface properties of the pore in which it resides, the droplets in smaller pores will remain while the larger pores are purged (assuming the surface properties are similar throughout the structure). After a large pore adjacent to a smaller pore is purged, the smaller pore empties into the larger pore by capillary transport. This is shown by the logarithmic decay in pressure gradient through the gas diffusion layer after the current load is removed (Fig. 3). Initially the pressure drop decreases quickly as the large pores are purged, and then the rate decreases as the smaller pores empty into the larger pores. It is expected that these small pores see less gas flow than the primary flow paths through the larger pores and in turn would have a less significant effect on pressure drop through the diffusion layer.

3.2. Distribution of local water accumulation

Neutron radiographs detail areas of water hold-up and uniformity of its distribution across the active area. This demonstrates the dynamics associated with the interdigitated design. Each radiograph pixel represents about 94.2 μm × 94.2 μm ± 0.5 μm of active area, thus yielding local water volume/mass measurements with high resolution.

Water accumulation in the channels was of interest to determine if gas channels were flooding. Fig. 7 represents the early portion of a load cycle where reaction water is

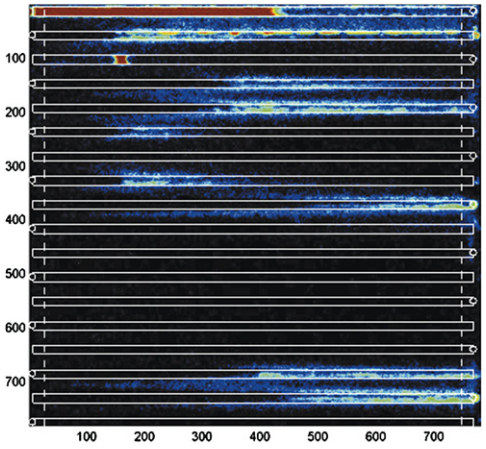

Fig. 7. Channel geometry overlay.

accumulating from a dry state due to the onset of load. A CAD drawing of the interdigitated cathode flow channels is imposed over the radiograph to illustrate areas of water accumulation (inlet manifold on left; outlet manifold on right). In Fig. 5 water droplets and films are shown to randomly accumulate in the outlet channels initially. As the experiment progresses, these water films form slugs that are periodically purged out of the cell. Contact line pinning due to the sharp transition from the outlet channel to the exhaust manifold is expected to be the root cause of accumulation at the end of each outlet channel.

Varying the inlet humidity of the cathode gas stream coupled with neutron imaging provides understanding of where and how much water can be removed in the vapor phase. These experiments show a significant decrease in accumulated liquid water as the cathode relative humidity is decreased from 100% to 50%. Fig. 8 presents the time transient of voltage, water mass, relative humidity, and ohmic resistance. The relative humidity was changed by increasing the cell temperature and the values shown in Fig. 8 were calculated based on a constant dew point of the inlet cathode gas.

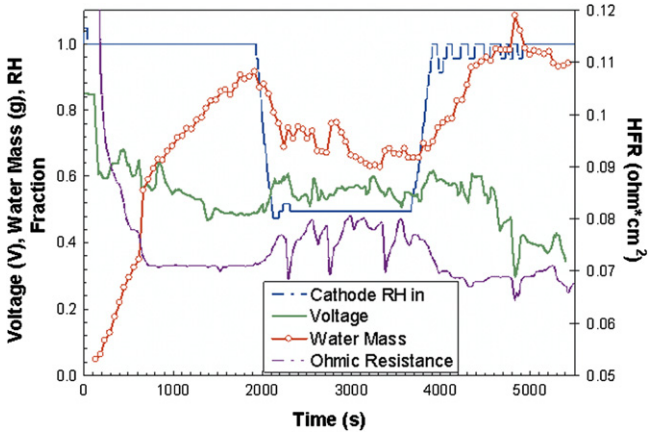

Fig. 8. Effect of cathode gas stream relative humidity on accumulated water mass.

During these experiments the ohmic resistance was measured with impedance spectroscopy at a frequency of 1.0 kHz. This resistance indicates the membrane's resistance to proton transfer, a function of membrane hydration. Fig. 8 shows this drying transient effect on ohmic resistance. The initial rapid decrease in ohmic resistance is proportional to the rate at which water is accumulated in the cell. The slope in ohmic resistance reached zero $\Omega\,cm^2/s$ after 10 min of cell operation, signifying the time constant for membrane hydration at this current load and water production rate. The instability in the ohmic resistance measurement correlates with rapid fluctuations in channel relative humidity. It has been observed that the negative "spikes" in high-frequency resistance (HFR) correspond to periodic slugs of product water that are purged through the channels or water slugs that are introduced from the humidifiers. Although great care was taken to remove excess liquid water from the inlet gas streams, there may be some condensation within the heated inlet gas lines due to local cold spots. The inlet hoses were oriented so that pooling of condensate would not occur and the dew point was calibrated with a dew cup at the heated line outlet. Over time this condensation can result in slugs of water moving through the fuel cell. The resulting HFR fluctuations are apparent under dry conditions where the membrane resistance is elevated above the fully saturated value and liquid water has greater influence on relative humidity.

It is apparent in all radiographs that the primary gas transport path is through channels and GDL located at vertical pixel 400–650. This region is shown to be consistently drier due to higher gas velocity. This local increase in velocity through the GDL and channels is a direct result of the pressure profile along the inlet and outlet headers.

3.3. In-plane permeability using pressure differential and saturation data

The in-plane permeability of the reactants in the gas diffusion layer is an important parameter to evaluate and correlate to fuel cell performance. Moreover, the behavior of this permeability with increasing volumetric water content can be evaluated with measured pressure differential and liquid water volume. These permeability functions for both the gas and liquid phases, represented by Darcy's equation, are important for multi-phase transport models in porous media. In the work presented below, only the gas phase permeability is investigated. A comprehensive model description is provided in Appendix A.

To evaluate the saturation only in the land regions of the fuel cell, the local water accumulation in the channel area is removed from the water mass data arrays. Then the remaining water mass is summed over the land portion of the active area. From this sum the estimated water mass for a fully hydrated membrane (0.05 ± 0.01 g for the land area only, assuming 30% water uptake by mass) is subtracted. With the assumption that no liquid water is located

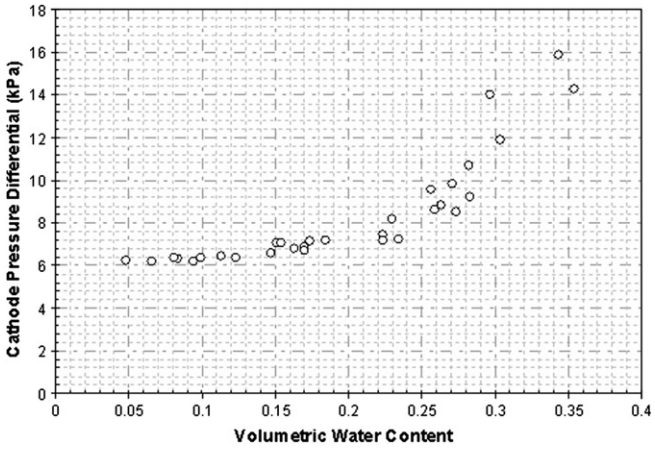

Fig. 9. Cathode pressure differential vs. diffusion layer saturation.

in the anode diffusion layer, electrodes, or microporous layers, the volumetric saturation fraction is calculated from the 75% porous, 166 μm thick compressed cathode diffusion layer substrate (not including MPL). The calculated saturation fractions thus consider all liquid water under the interdigitated lands to be located in the membrane and cathode diffusion layer.

The load cycling described in Section 3.1 combined with saturated inlet gas streams is ideal because evaporation can be ignored and back diffusion is minimized. The velocity profile through the depth of the cathode GDL is assumed to be uniform, an assumption that should be valid when the ratio of land width to GDL thickness is large. This ratio was 15 for these experiments. Calculations were applied to data after the current load was removed. Without water generation and species changes, convective flow through the cathode gas diffusion layer can be described by Darcy's law in the gas phase. Pressure drop through the channels was approximated using a friction factor based on the hydraulic radius of the rectangular channel. Appendix A describes how these assumptions can be used to calculate the permeability from the measured flow rate and pressure differential. Liquid water accumulation in the channels was calculated to have an insignificant impact on the measured pressure differential (<1%) as the pressure differential of the GDL will dominate the measurement. Plugged inlet channels may introduce error of up to 6% in calculated relative permeability if there is no gas flow through the plugged channel.

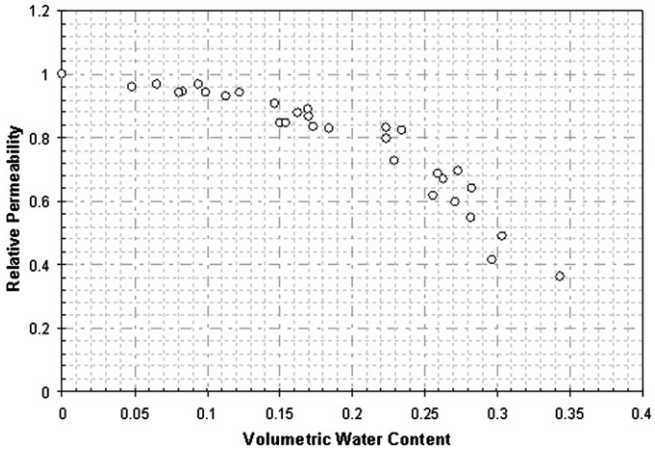

Fig. 10. Relative permeability vs. cathode GDL saturation.

From the cycle shown in Fig. 3, the cathode pressure differential as a function of saturation fraction is extracted from the region where the load was removed. Fig. 9 shows this measured pressure plotted against the saturation fraction in the cathode GDL substrate (calculated from measured water mass). The ratio $k(s)/k_0$ of permeability at a saturation level s to dry permeability is called the relative permeability. Using the model presented in Appendix A, the dry permeability was calculated from the steady state dry pressure drop of 6.0 kPa at a flow of 333 sccm, yielding a value of 0.26 Darcy (cm^2). Fig. 10 shows the plot of relative permeability as a function of cathode land saturation.

As described in Section 3.1 the critical void in the cathode diffusion medium is found to be $44.2 \pm 2.5\%$. Fig. 10 indicates that this volumetric water content reduces the gas permeability through the cathode GDL significantly. It is hypothesized that extrapolating this permeability curve shown in Fig. 10 will result in an asymptote near zero permeability once the cathode GDL void is over 50% full of liquid water.

4. Conclusions

Neutron radiography has been used to visualize liquid water distributions and measure average accumulated water mass during transient tests of a PEM fuel cell. An interdigitated flow field was used to force all cathode gas through the porous backing layers and the resulting changes in pressure differential from inlet to outlet have been shown to correlate with the saturation level of gas diffusion layers. Local water accumulation patterns and uniformity were illustrated. The cathode inlet humidity was demonstrated to have a substantial effect on liquid water accumulation. The following conclusions are drawn:

1. Small amounts of condensation in the gas handling system can have a significant effect on local channel flooding for small scale PEMFC experiments.
2. Initially, a relatively dry cathode accumulates liquid water at a rate equivalent to that at which it is produced.
3. The porous backing layers operating under saturated conditions accumulates water until a critical water mass is reached (approximately $44.2 \pm 2.5\%$ of available void volume); at this point reaction water is removed from the cell at the rate in which it is produced.
4. With the driving force for evaporation eliminated in the experiment and with no product water being produced, homogenous convective gas shear cannot account for slow water removal rate. It is hypothesized that gas is initially purged from large pores, and then capillary transport removes water trapped in smaller pores to empty through large pores.

5. Flooding occurs primarily in the outlet channels at the manifold due to pinning at the sharp transition from channel to manifold.
6. Ohmic loss measured with high frequency resistance is proportional to water accumulation in presented experiments. Both the mean value and temporal fluctuations are indicative of the hydration in the membrane and GDL.
7. Relative permeability is reduced significantly as the critical water mass is approached. Mass transport resistance will force the limiting current once half of the open void in the cathode GDL is full of liquid water.

Acknowledgements

This work was supported by the US Department of Commerce, the NIST Ionizing Radiation Division, the Director's office of NIST, the NIST Center for Neutron Research, and the Department of Energy interagency Agreement No. DE_AI01-01EE50660.

Appendix A. Interdigitated in-plane permeability calculation

The Fig. 11 schematic shows the interdigitated flow field. Each channel is dead-ended so that all gas must flow under lands between the inlet and outlet channels. For modeling purposes, it is assumed that the channels are placed in a periodic array with each inlet channel feeding the two adjacent outlet channels and each outlet channel being fed by the two adjacent inlet channels. The width and depth of each channel are given respectively as d_{ch} and h_{ch}. The land width is given as d_{land}. The height of the gas diffusion layer (GDL) is h. The length of each channel is l, and the x-axis is parallel to the channels with the inlets at $x = 0$ and the dead-ends of the inlet channels (and also the outlets) at $x = l$. For modeling purposes, we assume that the gas pressure in each channel cross section is uniform and that the flow under lands is proportional to the pressure difference at the point in question between the inlet and outlet channels. In addition, we assume that the gas pressure in the GDL at all points under a channel is equal to the pressure in the channel cross section. This assumption should be valid for a GDL that is much thinner than the land width. The gas velocity in the GDL under lands is therefore uniform, with no velocity variations between the flow field (at the top of the GDL) and the electrode (at the bottom of the GDL).

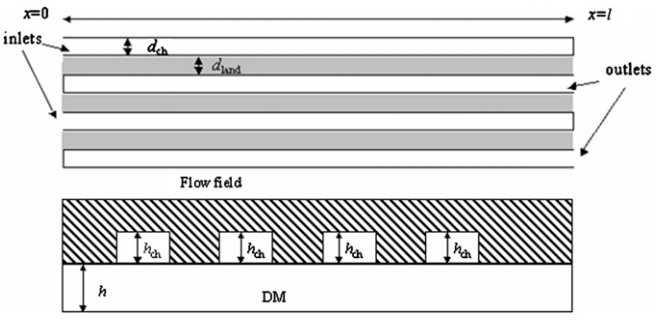

Fig. 11. Dimensioning parameters for interdigitated model.

Let $R_{ch} = d_{ch}h_{ch}/(d_{ch} + h_{ch})$ be the hydraulic radius of the channel. We designate the inlet channels with the subscript 1 and the outlet channels with the subscript 2. Let V_i be the average channel velocity in channel i at a point x. We use an approximate form of the Poisson equation

$$V_i = -\frac{R_{ch}^2}{8\mu}\nabla P_i = -\frac{R_{ch}^2}{8\mu l}P_i'(y), \tag{1}$$

where $y = x/l$ is a dimensionless variable and the prime indicates differentiation with respect to y. The velocity of gas flowing under the lands from an inlet to an outlet channel is given by

$$V_{land}(y) = -\frac{k}{\mu}\frac{(P_2(y) - P_1(y))}{d_{land}}, \tag{2}$$

where k is the permeability of the GDL and μ is the gas viscosity. We assume constant gas density in the channels and in the GDL. Then the conservation of mass dictates that

$$\begin{aligned} d_{ch}h_{ch}V_1'(y) &= -2hlV_{land}(y) = -\frac{2khl}{\mu d_{land}}(P_1(y) - P_2(y)) \\ &= -d_{ch}h_{ch}V_2'(y), \end{aligned} \tag{3}$$

where the factor $d_{ch}h_{ch}$ is the cross sectional area of the channel. We introduce a dimensionless pressure $\overline{P}_i(y) = (P_i(y) - P_2(1))/\Delta P$, where ΔP is the pressure drop from inlet to outlet. We thus have the boundary conditions

$$\overline{P}_1(0) = 1, \quad \overline{P}_1'(1) = 0, \quad \overline{P}_2(1) = 0 \quad \text{and} \quad \overline{P}_2'(0) = 0. \tag{4}$$

Eqs. (1) and (3) can now be combined into a dimensionless matrix form

$$\begin{bmatrix} \overline{P}_1'' \\ \overline{P}_2'' \end{bmatrix}(y) = \begin{bmatrix} \alpha & -\alpha \\ -\alpha & \alpha \end{bmatrix}\begin{bmatrix} \overline{P}_1 \\ \overline{P}_2 \end{bmatrix}(y), \tag{5}$$

where

$$\alpha = \frac{16khl^2}{d_{land}d_{ch}h_{ch}R_{ch}^2}.$$

The parameter α can be viewed as the ratio of convective resistance to gas flow in the channels divided by convective resistance to gas flow under lands.

Solutions will be in linear combinations of the two eigenfunctions

$$\begin{bmatrix} \overline{P}_1 \\ \overline{P}_2 \end{bmatrix} = \begin{bmatrix} F + G \\ F - G \end{bmatrix} \tag{6}$$

with

$$F(y) = A_1 y + A_2 \quad \text{and}$$
$$G(y) = A_3 \sinh\left(y\sqrt{2\alpha}\right) + A_4 \cosh\left(y\sqrt{2\alpha}\right). \tag{7}$$

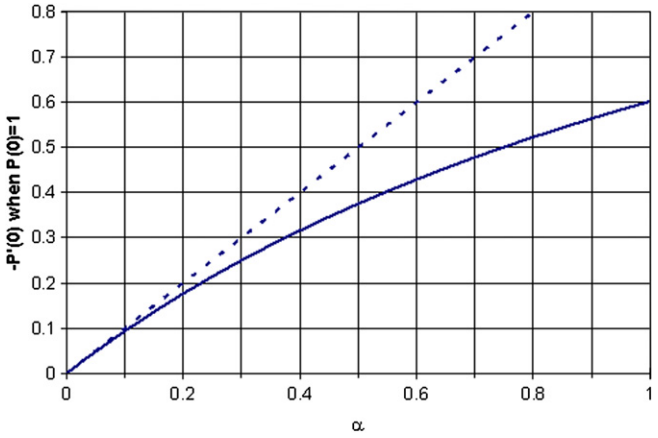

Fig. 12. Dimensionless inlet gas velocity vs. convective resistance to gas flow.

The boundary conditions (4) must be used to solve for the constants A_i. These constants take on the values

$$A_1 = -\frac{\beta \sinh[\beta]}{\cosh[\beta] + \beta \sinh[\beta]}$$

$$A_2 = 1 - \frac{\cosh[\beta]}{2(\cosh[\beta] + \beta \sinh[\beta])}$$

$$A_3 = -\frac{\sinh[2\beta]}{2(1 + \cosh[2\beta] + \beta \sinh[2\beta])}$$

$$A_4 = \frac{\cosh[\beta]}{2(\cosh[\beta] + \beta \sinh[\beta])}$$

where $\beta = \sqrt{\alpha/2}$. To evaluate data, we consider the quantity $-\overline{P}_1'(0)$, which can be viewed as a dimensionless inlet gas velocity, and we plot it as a function of α. This is shown in Fig. 12.

The dashed line in Fig. 12 indicates that, for small α, the curve has a slope of 1. This corresponds to the situation in which the GDL permeability is so low that there are no pressure losses in the channels. Instead the entire pressure drop occurs uniformly in the GDL between the inlet and outlet channels. As α increases, (as the GDL becomes more permeable) the pressure drops in the channels become comparable to those between the channels. As a result of this, the curve deviates from the diagonal line. One can show that in the limit of large α the derivative $\overline{P}_1'(0)$ tends to $-\sqrt{\alpha/2}$.

We turn now to the issue of determining a permeability k from pressure and flow data for the interdigitated flow field. We assume that steady-state conditions prevail and that the pressure drop ΔP and volumetric flow V^{vol} have both been measured. Then one finds that

$$V^{\text{vol}} = -\frac{n_{\text{ch}}}{2} \frac{d_{\text{ch}} h_{\text{ch}} R_{\text{ch}}^2 \Delta P}{8\mu l} \overline{P}_1'(0), \tag{8}$$

where n_{ch} is the number of cathode channels, only half of which are gas inlet channels. It follows that $\overline{P}_1'(0)$ can be determined from $\Delta P, V^{\text{vol}}$, and the other parameters in Eq. (8). From $\overline{P}_1'(0)$ we can use the above plot to extract a value for α, from which one can determine the permeability k. Fig. 12 was computed by starting with α-values and using them to calculate values for $-\overline{P}_1'(0)$. In applications, one starts with a value of $-\overline{P}_1'(0)$ and must compute a value of α associated to it. A bisection method was used to accomplish this task.

References

[1] T.V. Nguyen, A gas distributor design for proton-exchange-membrane fuel cells, J. Electrochem. Soc. 143 (1996) L105.
[2] D. Woods III, J. Yi, T.V. Nguyen, Effect of direct liquid water injection and interdigitated flow field on the performance of proton exchange membrane fuel cells, Electochim. Acta 43 (1998) 3795–3809.
[3] W. He, G. Lin, T.V. Nguyen, Diagnostic tool to detect electrode flooding in proton-exchange-membrane fuel cells, AIChE J. 49 (2003) 3221–3228.
[4] L. Wang, H. Liu, Performance studies of PEM fuel cells with interdigitated flow fields, J. Power Sources 134 (2004) 185–196.
[5] T.A. Trabold, J.P. Owejan, D.L. Jacobson, M. Arif, P.R. Huffman, In situ investigation of water transport in an operating PEM fuel cell using neutron radiography: Part 1 – Experimental method and serpentine flow field results, Int. J. Heat and Mass Transfer, in press, doi:10.1016/j.ijheatmasstransfer.2006.07.003.
[6] R.J. Bellows, M.Y. Lin, M. Arif, A.K. Thompson, D. Jacobson, Neutron imaging for in situ measurement of water transport gradients within Nafion in polymer electrolyte fuel cells, J. Electrochem. Soc. 146 (1999) 1099–1103.
[7] A.B. Geiger, A. Tsukada, E. Lehmann, P. Vontobel, A. Wokaun, G.G. Scherer, In situ investigation of two-phase flow in flow fields of PEFC's using neutron radiography, Fuel Cells 2 (2003) 92–98.
[8] D. Kramer, J. Zhang, R. Shimoi, E. Lehmann, A. Wokaun, K. Shinohara, G.G. Scherer, In situ diagnostic of two-phase flow phenomena in polymer electrolyte fuel cells by neutron imagining Part A. Experimental, data treatment, and quantification, Electrochimica Acta 60 (2005) 2603–2614.
[9] J.P. Owejan, Neutron radiography study of water transport in an operating fuel cell: effects of diffusion media and cathode channel properties, MS Thesis, Rochester Institute of Technology, Rochester, New York, 2003.
[10] N. Pekula, K. Heller, P.A. Chuang, A. Turhan, M.M. Mench, J.S. Brenizer, K. Unlu, Study of water distribution and transport in a polymer electrolyte fuel cell using neutron imaging, Nucl. Instr. Phys. Res. A 542 (2005) 134–141.
[11] R. Satija, D.L. Jacobson, M. Arif, S.A. Werner, In situ neutron imaging technique for evaluation of water management systems in operating PEM fuel cells, J. Power Sources 129 (2003) 238–245.
[12] D.S. Hussey, D.L. Jacobson, M. Arif, P.R. Huffman, R.E. Williams, J.C. Cook, Nucl. Instr. Phys. Res. A 542 (2005) 9–15.
[13] M. Mattes, E. Sartori, JEF Report 1 (1984).